

# Geophysical Research Letters<sup>®</sup>

## RESEARCH LETTER

10.1029/2021GL095619

### Key Points:

- Empirical linear correlation between reflected visible light intensity and *in situ* solute concentration
- Experimental determination of the critical Rayleigh-Darcy number for the onset of density-driven instability
- Experimental determination of the critical time scales for the onset of density-driven instability and convective dissolution

### Correspondence to:

C. Chen,  
cchen6@stevens.edu

### Citation:

Guo, R., Sun, H., Zhao, Q., Li, Z., Liu, Y., & Chen, C. (2021). A novel experimental study on density-driven instability and convective dissolution in porous media. *Geophysical Research Letters*, 48, e2021GL095619. <https://doi.org/10.1029/2021GL095619>

Received 13 AUG 2021

Accepted 17 NOV 2021

### Author Contributions:

**Conceptualization:** Yang Liu, Cheng Chen

**Data curation:** Hanxing Sun

**Formal analysis:** Ruichang Guo, Hanxing Sun, Qingqi Zhao, Zihao Li, Yang Liu, Cheng Chen

**Funding acquisition:** Cheng Chen

**Investigation:** Ruichang Guo, Hanxing Sun, Qingqi Zhao, Zihao Li, Yang Liu, Cheng Chen

**Methodology:** Ruichang Guo, Hanxing Sun, Qingqi Zhao, Zihao Li, Yang Liu, Cheng Chen

**Project Administration:** Cheng Chen

**Resources:** Yang Liu, Cheng Chen

**Software:** Ruichang Guo, Hanxing Sun



**Supervision:** Cheng Chen

**Validation:** Cheng Chen

**Writing – original draft:** Ruichang Guo, Cheng Chen

**Writing – review & editing:** Ruichang Guo, Hanxing Sun, Yang Liu, Cheng Chen

## A Novel Experimental Study on Density-Driven Instability and Convective Dissolution in Porous Media

Ruichang Guo<sup>1</sup>, Hanxing Sun<sup>2</sup>, Qingqi Zhao<sup>3</sup>, Zihao Li<sup>1</sup> , Yang Liu<sup>2</sup>, and Cheng Chen<sup>3</sup> 

<sup>1</sup>Department of Mining and Minerals Engineering, Virginia Tech, Blacksburg, VA, USA, <sup>2</sup>Department of Mechanical Engineering, Virginia Tech, Blacksburg, VA, USA, <sup>3</sup>Department of Civil, Environmental and Ocean Engineering, Stevens Institute of Technology, Hoboken, NJ, USA

**Abstract** Geological carbon dioxide (CO<sub>2</sub>) sequestration (GCS) in deep saline aquifers is a promising solution to mitigate the impact of anthropogenic CO<sub>2</sub> emissions on global climate change. CO<sub>2</sub> dissolved in formation water increases the solution density and can lead to miscible density-driven downward convection, which significantly accelerates the dissolution trapping of injected CO<sub>2</sub>. Experimental studies on miscible density-driven convection have been limited. In the laboratory, we found an empirical linear correlation between reflected green light intensity and solute concentration, which enabled *in situ* measurements of solute concentrations in the spatial and temporal domains and consequently the mass flux across the top boundary of the porous medium. Using the novel experimental techniques, we determined the critical Rayleigh-Darcy number and critical time scales for the onset of density-driven instability and convective dissolution. This is the first study to determine these critical system parameters using laboratory experiments.

**Plain Language Summary** Long-term storage of carbon dioxide (CO<sub>2</sub>) in geological formations, such as deep saline aquifers, is a promising solution to mitigate the impact of anthropogenic CO<sub>2</sub> emissions on global climate change. CO<sub>2</sub> dissolved in formation water increases the solution density and can lead to miscible density-driven downward convection, which accelerates the dissolution of CO<sub>2</sub> in formation water and thus improves the long-term security of the system. However, investigations of the critical system parameter and critical time scales for triggering downward convection have relied heavily on numerical simulations because of the challenges associated with laboratory experiments. In this study, we used experimental methods to find an empirical linear correlation between reflected visible light intensity and solute concentration, which enabled *in situ* measurements of solute concentrations in the spatial and temporal domains. Using these novel experimental techniques, we determined the critical Rayleigh-Darcy number and critical time scales for the onset of density-driven instability and convective dissolution. The findings from this experimental study have practical applications in many other engineered and natural processes, such as geothermal convection, heat transfer due to subsurface nuclear waste disposal, and variable-density groundwater flow.

## 1. Introduction

When a layer of viscous fluid is confined between two horizontal boundaries and heated from below, the fluid near the bottom boundary expands, leading to reduced density and a net buoyancy force in the opposite direction of the gravity. When the temperature difference between the top and bottom boundaries exceeds a certain threshold, the denser fluid near the top boundary penetrates downward, resulting in density-driven downward convection. This process is referred to as the Rayleigh-Bénard convection and was first studied by Rayleigh (1916) and Jeffreys (1926). If a porous medium saturated with a fluid is heated at the bottom boundary, similar instability can occur, which was first studied by Horton and Rogers (1945) and Lapwood (1948) and is referred to as the Rayleigh-Darcy or Horton-Rogers-Lapwood instability.

Fluid density variation can also be caused by solute transport. One example is geological carbon sequestration (GCS), which is permanent disposal of CO<sub>2</sub> in geological formations and has been considered a promising solution to reduce continuous CO<sub>2</sub> buildup in the atmosphere. Geological formations for CO<sub>2</sub> injection include deep coal beds, depleted oil and gas reservoirs, deep-sea sediments, and deep saline aquifers (Bergman & Winter 1995; Bruant et al., 2002; Celia et al., 2015; Ennis-King et al., 2005; Ennis-King & Paterson, 2005; Guo et al., 2020; House et al., 2006; Kovscek & Wang, 2005). Saline aquifers are preferable for GCS because they have the highest storage capacity globally (Bruant et al., 2002). When CO<sub>2</sub> is injected into deep saline aquifers with a

pressure higher than 73.8 bar and temperature higher than 31.0°C, it exists in the supercritical phase. Injected supercritical CO<sub>2</sub> (scCO<sub>2</sub>) migrates upward due to the buoyancy until it is stopped by the low-permeability cap rock. Meanwhile, scCO<sub>2</sub> dissolves in brine. Brine saturated with dissolved CO<sub>2</sub> has a density increase around 10 kg/m<sup>3</sup> (Chen et al., 2013; Chen & Zhang, 2010; Ennis-King et al., 2005). Increased brine density near the scCO<sub>2</sub>-brine interface can cause miscible density-driven downward convection, which is favorable for improving the long-term security of CO<sub>2</sub> storage. This CO<sub>2</sub> trapping mechanism is referred to as convective mixing (Chen et al., 2013) or convective dissolution (Neufeld et al., 2010). Convective dissolution drives dissolved CO<sub>2</sub> away from the scCO<sub>2</sub>-brine interface, which accelerates subsequent scCO<sub>2</sub> dissolution and thus facilitates the overall mass transfer rate from scCO<sub>2</sub> to brine. Our previous pore-scale study (Chen & Zhang, 2010) confirmed that CO<sub>2</sub> mass transfer by means of convective mixing is significantly faster than that driven by pure molecular diffusion. Sathaye et al. (2014) used geophysical and geochemical data to show that convective mixing in the Bravo Dome, a large natural CO<sub>2</sub> field in New Mexico, led to a CO<sub>2</sub> mass flux of 0.1 g/(m<sup>2</sup> yr); this work provided field evidence of convective mixing. In contrast, the convective CO<sub>2</sub> mass flux at the Sleipner Field in Norway was estimated as high as 20 kg/(m<sup>2</sup> yr) due to its much higher formation permeability.

There are several critical system parameters that regulate the behaviors of miscible density-driven convection. The first is the Rayleigh-Darcy number ( $Ra$ ), which is a dimensionless number that describes the ratio of gravitational instability to molecular diffusion. Density-driven instability can only occur when  $Ra$  exceeds a certain threshold value, which is referred to as the critical  $Ra$  number,  $Ra_{cr}$ . When  $Ra$  is higher than  $Ra_{cr}$ , the next question is how long it takes to trigger density-driven instability and convective dissolution. Due to the challenges associated with laboratory experiments, existing studies on  $Ra_{cr}$  and the critical times for triggering density-driven instability and convective dissolution relied heavily on stability analysis (Bestehorn & Firoozabadi, 2012; Cheng et al., 2012; Emami-Meybodi, 2017; Ennis-King et al., 2005; Ennis-King & Paterson, 2005; Hassanzadeh et al., 2006; Javaheri et al., 2010; Kim, 2013, 2014a, 2014b; Kim & Choi, 2012; Kim et al., 2008; Meulenbroek et al., 2013; Riaz et al., 2006; Slim & Ramakrishnan, 2010; Wessel-Berg, 2009; Xu et al., 2006) and direct numerical simulations (Azin et al., 2013; Chen et al., 2013; Elenius & Johannsen, 2012; Farajzadeh et al., 2007; Pau et al., 2010; Riaz et al., 2006; Slim, 2014; Wen et al., 2018).

Typical experimental methods for studying miscible density-driven convection include pressure-volume-temperature (PVT) cells (Moghaddam et al., 2012; Mojtaba et al., 2014; Newell et al., 2018; Shi et al., 2018) and Hele-Shaw cells (Kneafsey & Pruess, 2010; Neufeld et al., 2010; Taheri et al., 2017). PVT cells allow for assessment of CO<sub>2</sub> dissolution fluxes by measuring the pressure decay. Liyanage et al. (2019) used X-ray computed tomography technologies to investigate density-driven convection in a methanol-ethylene-glycol (MEG)/water system. *In situ* measurements of dissolved solute concentration can be conducted by measuring the color intensity of the solution in pure water (Slim et al., 2013) or porous media (Sahu & Neufeld, 2020). However, no prior experiments were able to determine  $Ra_{cr}$  and the relevant critical time scales due to the challenges in capturing flow dynamics at the initial stage of density-driven convection.

In this study, we developed a novel experimental setup, which allowed for both visual observations of density-driven convection and quantitative measurements of spatial-temporal distributions of solute concentrations in porous media. Particularly, we used the intensity of reflected visible light to infer the *in situ* solute concentration in porous media, allowing the use of an adequately thick sand box, which featured the primary novelty of this work. This is the first study to determine  $Ra_{cr}$  and the relevant critical time scales using laboratory experiments.

## 2. Theories and Mathematical Model

Migration of dissolved CO<sub>2</sub> in a homogeneous and isotropic porous medium can be modeled using the following equations with the Boussinesq approximation which assumes that the CO<sub>2</sub> concentration affects only the body force term (Chen et al., 2013):

$$\frac{\mu}{k} \mathbf{u} = -\nabla p + \rho g \mathbf{e}_y \quad (1)$$

$$\nabla \cdot \mathbf{u} = 0 \quad (2)$$

$$\phi \frac{\partial C}{\partial t} + \mathbf{u} \cdot \nabla C = \phi D \nabla^2 C \quad (3)$$

$$\rho = \rho_0(1 + \beta C) \quad (4)$$

where  $\mu$  is the fluid dynamic viscosity,  $k$  is the porous medium permeability,  $\mathbf{u}$  is the Darcy velocity vector,  $p$  is the fluid pressure,  $\rho$  is the fluid density,  $g$  is the gravitational acceleration,  $\mathbf{e}_y$  is the unit vector in vertical direction,  $C$  is the dissolved  $\text{CO}_2$  concentration,  $\phi$  is the porous medium porosity,  $D$  is the effective diffusivity of dissolved  $\text{CO}_2$  in the porous medium,  $\rho_0$  is the density of pure water, and  $\beta$  is the expansion coefficient and equal to  $0.001 \text{ m}^3/\text{kg}$ , which indicates that a dissolved  $\text{CO}_2$  concentration of  $1 \text{ kg}/\text{m}^3$  will increase the solution density by  $0.1\%$  (i.e.,  $1 \text{ kg}/\text{m}^3$ ).

The characteristic parameters are  $L_c = H$ ,  $u_c = \phi D/H$ ,  $C_c = C_0$ ,  $p_c = \mu \phi D/k$ , and  $t_c = H^2/D$ , where  $H$  is the depth of the porous medium in the sand box;  $C_0$  is the saturated  $\text{CO}_2$  concentration in the solution. The dimensionless variables are then defined as  $x^* = x/L_c$ ,  $y^* = y/L_c$ ,  $\mathbf{u}^* = \mathbf{u}/u_c$ ,  $C^* = C/C_c$ ,  $p^* = p/p_c$ , and  $t^* = t/t_c$ . After normalization, Equations 1–3 can be re-written in the dimensionless form:

$$\mathbf{u}^* = -\nabla p^* + Ra C^* \mathbf{e}_y \quad (5)$$

$$\nabla \cdot \mathbf{u}^* = 0 \quad (6)$$

$$\frac{\partial C^*}{\partial t^*} + \mathbf{u}^* \cdot \nabla C^* = \nabla^2 C^* \quad (7)$$

where  $Ra$  in Equation 5 is written as  $Ra = \Delta \rho g k H / (\rho_0 \phi \nu D)$ , where  $\Delta \rho$  is the density difference between  $\text{CO}_2$ -saturated solution and pure water, calculated as  $\Delta \rho = \rho_0 \beta C_0$ , and  $\nu$  is the kinematic viscosity. The maximum solution density increase,  $\Delta \rho$ , is  $10 \text{ kg}/\text{m}^3$  because the dissolved  $\text{CO}_2$  concentration in the saturation state,  $C_0$ , is  $10 \text{ kg}/\text{m}^3$  (Chen et al., 2013). The higher the value of  $Ra$ , the more likely that density-driven instability and convective dissolution will be triggered.

### 3. Experimental Methods and Materials

The experiments were carried out in a  $0.8 \text{ m} \times 0.8 \text{ m} \times 0.018 \text{ m}$  quasi-two-dimensional (2D) sand box fabricated with transparent acrylic panels, which enabled visual observations of the transport processes in the porous medium. The sand in the box was initially saturated with pure water. MEG and pure water were mixed to mimic a solution saturated with dissolved  $\text{CO}_2$ , which was then injected into the top fluid reservoir to trigger miscible density-driven convection. A porous mesh sheet was placed on the top of the sediment bed to prevent sand particle movement. Overlying the porous mesh sheet was an impermeable panel, which eliminated the impact of fluid flow when the MEG solution was injected into the top fluid reservoir. After the reservoir was filled with the MEG solution, the impermeable panel was removed to allow MEG to migrate into the sand box through molecular diffusion. Figure 1a illustrates the experimental setup.

The density of a MEG-water solution can be either higher or lower than pure water, depending on the MEG mass concentration in the solution (Liyanage et al., 2019; Neufeld et al., 2010). In this work, we used MEG having a 60 wt% ethylene-glycol content. Figure 1b illustrates the measured MEG solution density as a function of MEG concentration. The MEG solution density increased approximately linearly with the MEG mass concentration, and it reached the maximum when the MEG concentration was 50%. In addition, at a MEG concentration of 50%, the MEG solution density was higher than water by  $11 \text{ kg}/\text{m}^3$ , which is approximately equal to the density increase in a  $\text{CO}_2$ -saturated solution (Chen et al., 2013). This implies that the maximum increased gravitational acceleration due to the dissolved MEG, calculated as  $\Delta \rho g / \rho_0$ , was around  $0.1 \text{ m}/\text{s}^2$ , which is the same as that in a  $\text{CO}_2$ -saturated solution. Therefore, we placed a MEG solution having a 50% mass concentration in the fluid reservoir as an analogue of  $\text{CO}_2$ -saturated solution at the top boundary. The porous media in the sand box were constructed using pure silica sand. Table 1 illustrates the sand properties. In this study,  $Ra$  ranged from 481 to 7,959, which was within the relevant range associated with field-scale saline aquifers (Liyanage et al., 2019).

The MEG solution in the top fluid reservoir was dyed with a blue tracer. A high-speed high-resolution digital camera and two panel light sources were placed at the front side of the sand box to take pictures. Most experiments calibrated the relationship between solute concentration and transmitted light intensity, which requires that the thickness of the sand box (Sahu & Neufeld, 2020) or Hele-Shaw cell (Slim et al., 2013) be adequately small to allow for light penetration. This may cause wall effects on flow dynamics. Thus, we calibrated the relationship between the MEG mass concentration and intensities of the reflected red, green, and blue light, as shown in

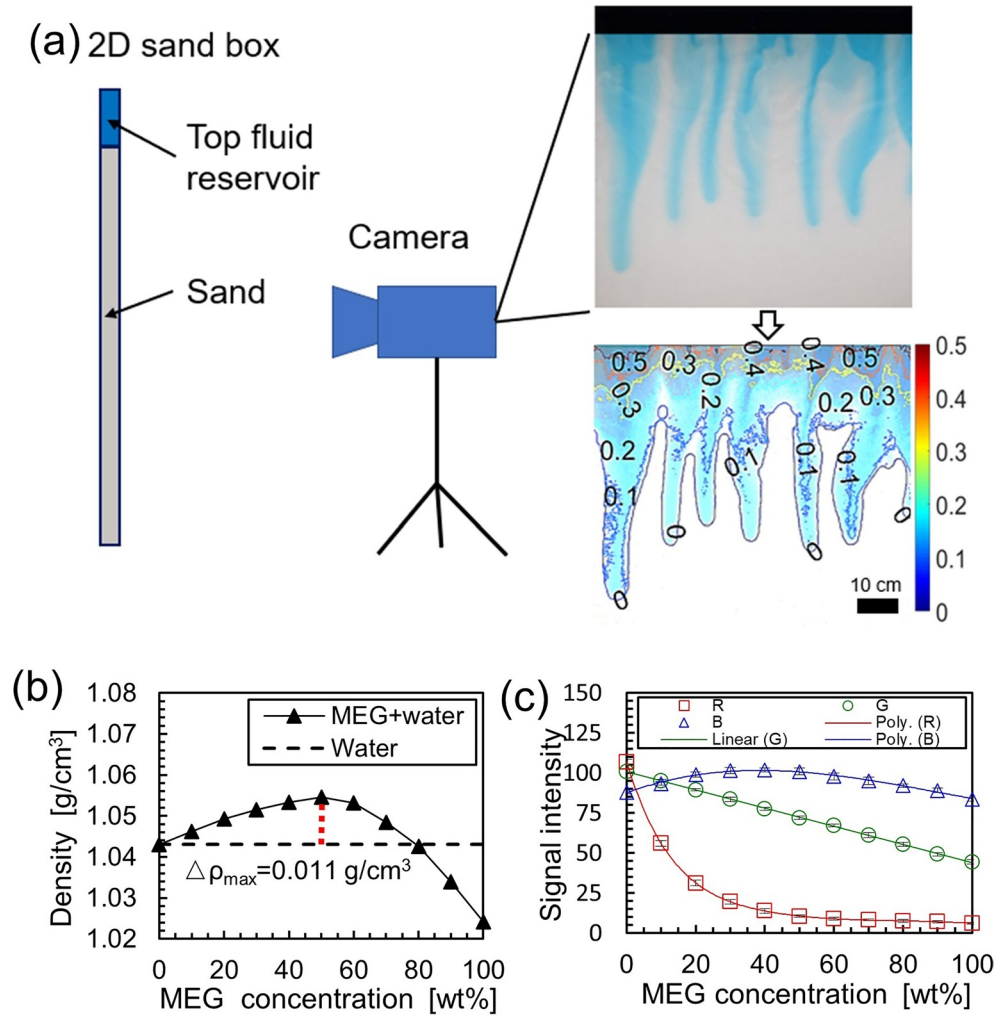


**Figure 1.** (a) Schematic plot of the experimental setup. (b) Density of MEG-water solution as a function of MEG mass concentration. (c) Signal intensity of the red, green, and blue light as a function of MEG mass concentration. The scatter data points are experimental data fitted with the solid curves.

Figure 1c, allowing the use of an adequately thick sand box. It was observed that the intensities of the reflected red and green light signals decreased with an increasing MEG mass concentration, because a higher MEG concentration absorbed more red and green light. We used the green light signal to infer the MEG mass concentration because of the linear relationship between them. Because the green light intensity on each individual pixel can be obtained, the MEG mass concentration at the same pixel can be calculated, which enabled us to obtain the

MEG concentration distribution over the entire 2D domain. The distribution of the dimensionless concentration,  $C^*$ , was obtained by normalizing the MEG concentration distribution with the initial MEG concentration in the fluid reservoir, as shown in Figure 1a. The signal intensity-MEG concentration correlation shown in Figure 1c was measured before each experiment to eliminate the influence of a possible background light change. The following linear correlation was found:

$$C = aI_G + b \quad (8)$$

where  $C$  is MEG mass concentration and  $I_G$  is green-channel signal intensity. The values of  $a$  and  $b$  were fitted as  $-0.0179 \pm 0.0014$  and  $1.7946 \pm 0.0996$ , respectively.

**Table 1**  
Properties of Sand Used in the Experiments

Sand mesh size	Average grain size ( $\mu\text{m}$ )	Permeability ( $\times 10^{-12} \text{ m}^2$ )	Porosity	$Ra$
#12–20	1,144	49.00	0.325	7,959
#16–30	768	29.90	0.345	4,723
#20–40	499	15.00	0.369	2,404
#40–70	285	5.37	0.357	944
#50–80	250	4.38	0.416	481

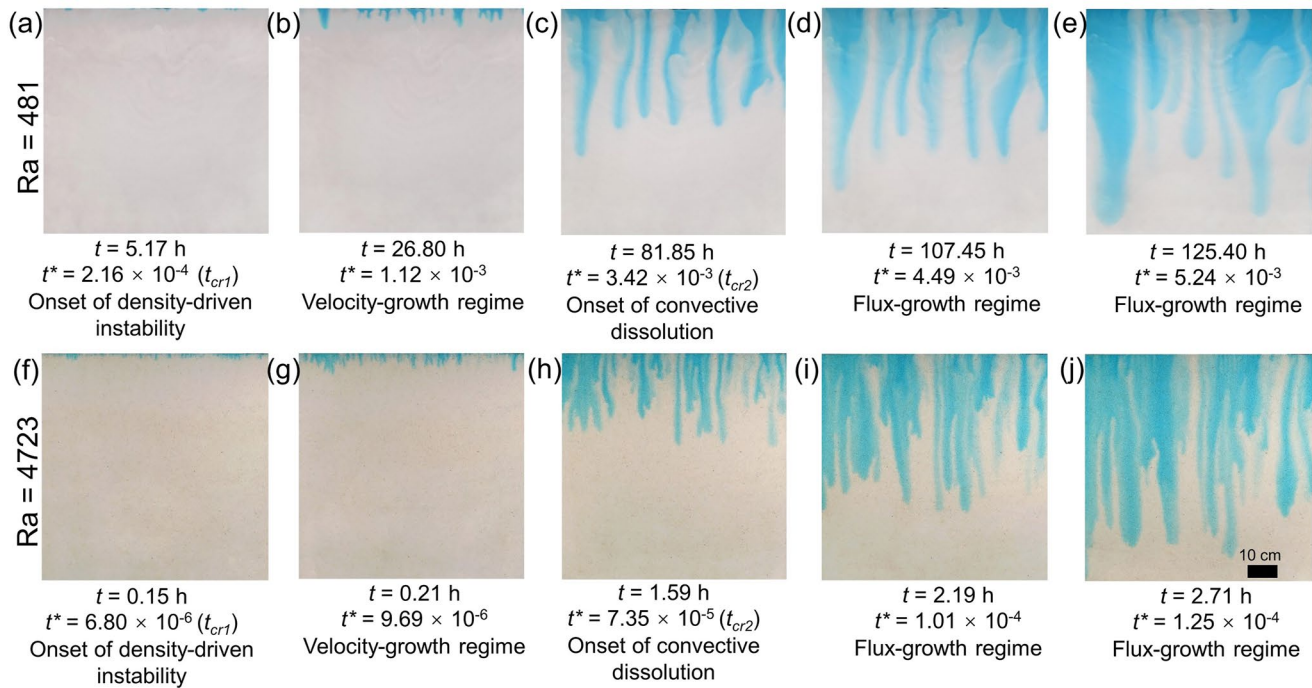


**Figure 2.** Development of density-driven instability and convective dissolution for  $Ra = 481$  (a–e) and  $Ra = 4,723$  (f–j). Blue fingers indicate density-driven downward penetration of MEG-rich solution.

## 4. Results and Discussion

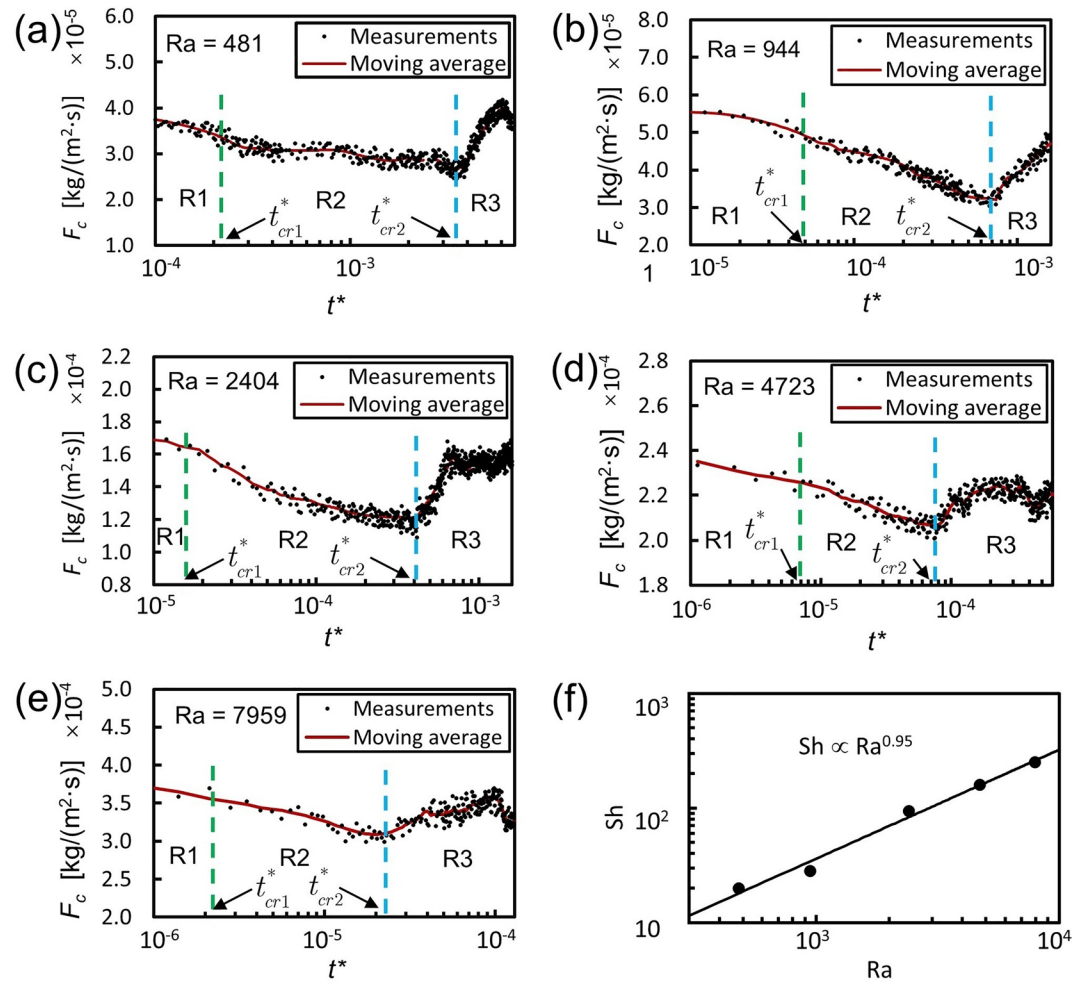
### 4.1. Overview of Density-Driven Instability and Convective Dissolution

Figure 2 illustrates the transition from a diffusion-dominated process to a convection-dominated process in the experiments, which can be classified into three stages, including the diffusive regime, velocity-growth regime, and flux-growth regime. In the diffusive regime, MEG mass transfer was controlled primarily by molecular diffusion. With the accumulation of instability at the top interface, the onset of density-driven instability led to local convective mass transfer at the penetration front. The critical time for the onset of density-driven instability,  $t_{cr1}$ , was defined as the time when the peak downward velocity grew to a level that was one order of magnitude higher than the diffusion-regulated characteristic velocity; this critical time marked the end of the diffusive regime and the beginning of the velocity-growth regime.

In the velocity-growth regime the overall MEG mass transfer from the top fluid reservoir to the underlying porous medium was still dominated primarily by molecular diffusion. Therefore, the overall MEG mass flux continuously decayed at early times because mass transferred into the underlying porous medium diminished the concentration gradient across the interface, which hampered diffusive mass transfer. At a later time, MEG-rich fingers were adequately developed, and consequently the mass flux contributed by convection started to dominate over the mass flux contributed by pure molecular diffusion. At this point, the total MEG mass flux started to increase. The time when the total MEG mass flux started to increase was the critical time for the onset of convective dissolution,  $t_{cr2}$ , which marked the end of the velocity-growth regime and the beginning of the flux-growth regime.

### 4.2. Mass Transfer Rate

Using the signal intensity-MEG concentration relationship, the MEG concentration distribution over the entire 2D porous medium was determined, based on which the total MEG mass transferred across the top interface can be calculated by integrating the MEG concentration within the 2D domain. The MEG mass flux ( $\text{kg}/\text{m}^2/\text{s}$ ), defined as MEG mass transferred across a unit interfacial area per unit time, was calculated as the total MEG mass increment in the porous medium over two consecutive measurement times normalized by the total interfacial area and the time increment.



**Figure 3.** MEG mass flux across the top boundary as a function of dimensionless time for (a)  $Ra = 481$ , (b)  $Ra = 944$ , (c)  $Ra = 2,404$ , (d)  $Ra = 4,723$ , and (e)  $Ra = 7,959$ . The green dash line indicates the dimensionless onset time for density-driven instability,  $t_{cr1}^*$ . The blue dash line indicates the dimensionless onset time for convective dissolution,  $t_{cr2}^*$ . The two onset times divide the transition stage into three regimes, which are the diffusive regime (R1), velocity-growth regime (R2), and flux-growth regime (R3). (f) Power-law relationship between  $Sh$  and  $Ra$ .

Figures 3a–3e demonstrate the MEG mass flux as a function of dimensionless time under various  $Ra$  numbers. The dimensionless time is defined as  $t^* = t/t_c$ , where  $t$  is the experimental time (s) and  $t_c$  is the characteristic time (s). The MEG mass flux decreased first and then increased. This was due to a competing process between diffusive mass transfer and convective mass transfer. In the early stages (i.e., diffusive regime and velocity-growth regime), MEG mass transfer from the top fluid reservoir to the underlying porous medium was dominated primarily by molecular diffusion. Although the onset of density-driven instability led to local convective mass transfer at the penetration front, the overall mass flux across the interface was still dominated primarily by molecular diffusion. The MEG mass transported into the porous medium reduced the concentration gradient across the top interface, which hampered the mass flux contributed by pure molecular diffusion. This explained the continuous decay of MEG mass flux in the early stages. At a later time, MEG-rich fingers were adequately developed, and consequently the mass flux contributed by convection started to dominate over the mass flux contributed by molecular diffusion. At this point, the total MEG mass flux started to increase even the mass flux contributed by pure molecular diffusion was continuously diminished. The time when the total MEG mass flux started to increase was the critical time for the onset of convective dissolution (i.e., onset of the flux-growth regime).

The ratio of convective mass flux to diffusive mass flux was described using the Sherwood number ( $Sh$ ), a dimensionless number defined as  $Sh = F_c / (\phi \Delta C D / H)$ , where the value of MEG mass flux,  $F_c$ , was calculated as the average over the entire temporal domain, and  $\Delta C$  was the difference between the MEG concentration in

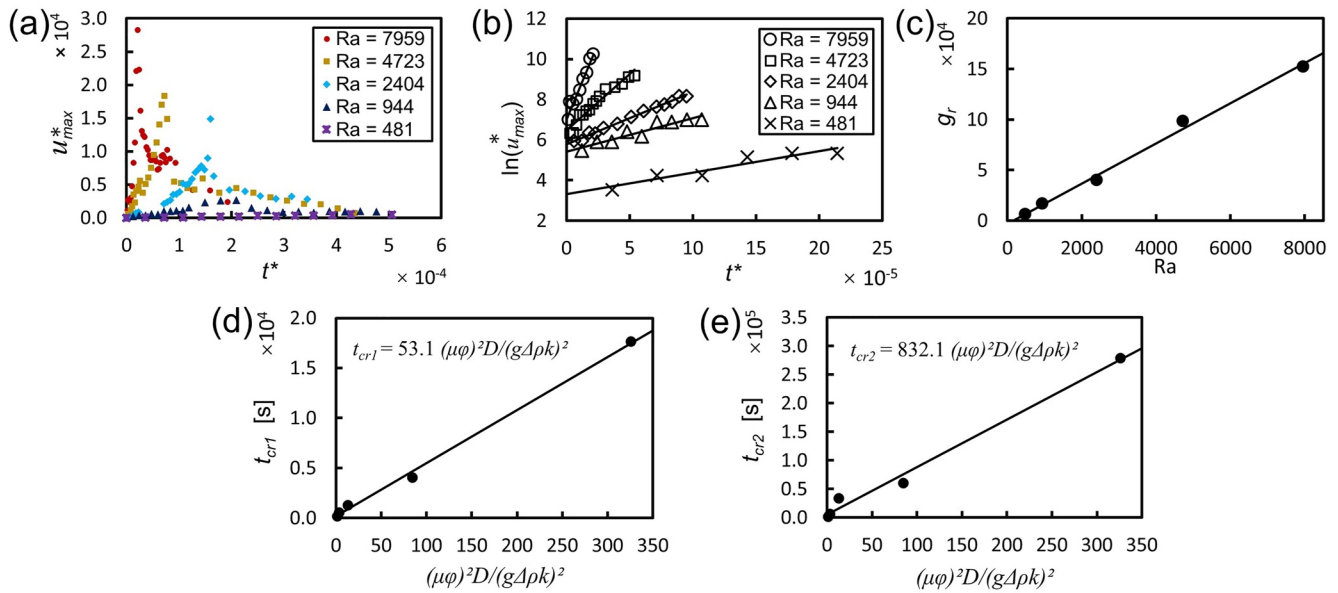


**Figure 4.** (a) Normalized peak downward velocity as a function of dimensionless time. (b) Fitting natural logarithm of dimensionless peak downward velocity at early times. (c) Growth rate of peak downward velocity as a function of  $Ra$ . The intersection of the extrapolation line with the  $x$  axis corresponds to  $Ra = 259$ , which is the  $Ra_{cr}$ . Critical times for the onset of (d) density-driven instability. (e) Convective dissolution as a function of  $(\mu\phi)^2 D / (g\Delta\rho k)^2$ .

the top fluid reservoir (i.e.,  $C_0$ ) and MEG concentration in pure water (i.e., zero). Figure 3f illustrates that the experimental measurements showed a power-law correlation between  $Sh$  and  $Ra$ , written as  $Sh \propto Ra^{0.95}$ , which was consistent with previous experimental studies (Liyanage et al., 2019; Neufeld et al., 2010).

### 4.3. Peak Downward Velocity

Previous numerical studies (Chen et al., 2013; Chen & Zhang, 2010) on miscible density-driven convection showed that the peak downward velocity occurs at the penetration front. Therefore, we used digital image tracking methods (Fu & Liu, 2016) to find the downward velocities on the MEG-rich penetration front, and the maximum downward velocity on the penetration front was the peak downward velocity. Figure 4a illustrates the dimensionless peak downward velocity as a function of dimensionless time. The dimensionless peak downward velocity is defined as  $u_{max}^* = u_{max} / u_c$ , where  $u_{max}$  is the peak downward velocity and  $u_c$  is the characteristic velocity.

Figure 4a demonstrated that under a higher  $Ra$  number the peak downward velocity reached its maximum value earlier. The non-monotonic evolution of the peak downward velocity was caused by a competing process between the convection of dissolved MEG and transverse dispersion. During downward penetration, transverse dispersion decreased the concentration gradient across the finger front and thus reduced the density difference, which hampered the downward convection and thus reduced the peak downward velocity. After the peak downward velocity reached its maximum value, it gradually decreased to a relatively low level. In some cases, especially under a high  $Ra$ , the later-time peak downward velocity can approach zero.

### 4.4. Critical $Ra$

Our previous numerical study found that  $Ra_{cr} = 250$  in a homogeneous and isotropic aquifer (Chen et al., 2013). However, due to the challenges in measuring *in situ* solute concentration and flow velocities in the laboratory, there were no existing experimental studies in determining the  $Ra_{cr}$  in the laboratory. Based on our study (Chen et al., 2013), when density-driven instability is triggered, the peak downward velocity grows exponentially with time. Therefore, exponential functions were used to fit the peak downward velocities in the increasing stage (i.e., at early times). Figure 4b demonstrates the natural logarithm of the dimensionless peak downward velocity as a function of the dimensionless time. The linear correlations confirm that  $u_{max}^* \propto \exp(g_r t^*)$  in the early stage of instability development. Therefore, the slopes of the linear relationships in Figure 4b are the growth rates of the

peak downward velocities. Figure 4c illustrates the velocity growth rate as a function of  $Ra$ . The growth rate decreased approximately linearly with the decrease of  $Ra$ . When the growth rate approached zero, the corresponding  $Ra$  was considered as the  $Ra_{cr}$ , which was found as 259 in this experiment.

#### 4.5. Correlations for Critical Times

In this study, the critical time for triggering density-driven instability,  $t_{cr1}$ , was determined using the following equation:

$$u_{max} = u_c \exp(g_r t) \quad (9)$$

where the value of the velocity growth rate,  $g_r$ , was known based on the measurements shown in Figure 4b. The value of  $t_{cr1}$  was the  $t$  value that gave  $u_{max} = 10u_c$ , which was the time when the peak downward velocity grew to a level one order of magnitude higher than the diffusion-regulated characteristic velocity. It should be noted that  $t_{cr1}$  is usually too short to directly determine in laboratory experiments (Mahmoodpour et al., 2019; Mojtaba et al., 2014; Newell et al., 2018; Shi et al., 2018). Therefore, we determined  $t_{cr1}$  using Equation 9, which was based on the extrapolation in the temporal domain.

The determined  $t_{cr1}$  values and the corresponding sand permeability values,  $k$ , were used to fit the following empirical correlation based on the formulation found in our previous study (Chen et al., 2013):

$$t_{cr1} = C_1 \frac{(\mu\phi)^2 D}{(g\Delta\rho k)^2} \quad (10)$$

where  $C_1$  is a constant. Figure 4d illustrates that the data fitting of the laboratory experimental data found  $C_1 = 53.1$ . Xu et al. (2006) found  $C_1 = 75.2$  using linear stability analysis with periodic-wave perturbations. Slim and Ramakrishnan (2010) found  $C_1 = 47.9$  using linear stability analysis with infinitesimal perturbations. Chen et al. (2013) found  $C_1 = 61.1$  using direct numerical simulations.

The  $t_{cr2}$  values determined from the mass flux plots (i.e., Figure 3) and the corresponding sand permeability values,  $k$ , were used to fit the following empirical correlation:

$$t_{cr2} = C_2 \frac{(\mu\phi)^2 D}{(g\Delta\rho k)^2} \quad (11)$$

where  $C_2$  is a constant. Figure 4e illustrates that the data fitting found  $C_2 = 832.1$ . Emami-Meybodi et al. (2015) reviewed previous numerical studies and showed that the value of  $C_2$  ranged from 500 to 5,619, depending on different initial perturbations. Our study is the first to experimentally determine  $C_2$  in the laboratory. The value of  $C_2$  is more than one order of magnitude larger than  $C_1$ , which suggests that the critical time for triggering convective dissolution is longer than that for triggering density-driven instability by more than one order of magnitude.

## 5. Conclusion and Implications

We experimentally investigated density-driven instability and convective dissolution in a 2D sand box. We found a linear relationship between MEG mass concentration and reflected green light intensity, which enabled *in situ* measurements of solute concentrations in the spatial and temporal domains and consequently the mass flux across the top boundary. The  $Ra_{cr}$  and critical time scales for the onset of density-driven instability and convective dissolution were determined. This is the first study to determine these critical system parameters using novel laboratory experiments, which provides datasets for evaluating initial perturbations in numerical models. In practice, the determination of  $t_{cr2}$  has important applications in field-scale GCS because it marks a crucial moment when the overall dissolved  $CO_2$  mass flux starts to accelerate due to density-driven convection. This study also has applications in geothermal convection, heat transfer due to subsurface nuclear waste disposal, and variable-density groundwater flow. Future laboratory studies are needed to investigate the role of permeability heterogeneity on density-driven instability and convective dissolution.



## Data Availability Statement

Data are available through: <https://doi.org/10.5281/zenodo.5196676>.

## Acknowledgments

The authors are thankful to the financial support provided by the United States National Science Foundation's Division of Earth Sciences under the award number of EAR-1921601.

## References

- Azin, R., Raad, S. M. J., Osfouri, S., & Fatehi, R. (2013). Onset of instability in CO<sub>2</sub> sequestration into saline aquifer: Scaling relationship and the effect of perturbed boundary. *Heat and Mass Transfer*, *49*, 1603–1612. <https://doi.org/10.1007/s00231-013-1199-7>
- Bergman, P. D., & Winter, E. M. (1995). Disposal of carbon-dioxide in aquifers in the US. *Energy Conversion and Management*, *36*, 523–526. [https://doi.org/10.1016/0196-8904\(95\)00058-L](https://doi.org/10.1016/0196-8904(95)00058-L)
- Bestehorn, M., & Firoozabadi, A. (2012). Effect of fluctuations on the onset of density-driven convection in porous media. *Physics of Fluids*, *24*, 114102. <https://doi.org/10.1063/1.4767467>
- Bruant, R. G., Celia, M. A., Guswa, A. J., & Peters, C. A. (2002). Safe storage of CO<sub>2</sub> in deep saline aquifers. *Environmental Science & Technology*, *36*, 240a–245a. <https://doi.org/10.1021/es0223325>
- Celia, M. A., Bachu, S., Nordbotten, J. M., & Bandilla, K. W. (2015). Status of CO<sub>2</sub> storage in deep saline aquifers with emphasis on modeling approaches and practical simulations. *Water Resources Research*, *51*, 6846–6892. <https://doi.org/10.1002/2015wr017609>
- Chen, C., Zeng, L., & Shi, L. (2013). Continuum-scale convective mixing in geological CO<sub>2</sub> sequestration in anisotropic and heterogeneous saline aquifers. *Advances in Water Resources*, *53*, 175–187. <https://doi.org/10.1016/j.advwatres.2012.10.012>
- Chen, C., & Zhang, D. X. (2010). Pore-scale simulation of density-driven convection in fractured porous media during geological CO<sub>2</sub> sequestration. *Water Resources Research*, *46*. <https://doi.org/10.1029/2010wr009453>
- Cheng, P., Bestehorn, M., & Firoozabadi, A. (2012). Effect of permeability anisotropy on buoyancy-driven flow for CO<sub>2</sub> sequestration in saline aquifers. *Water Resources Research*, *48*. <https://doi.org/10.1029/2012wr011939>
- Elenius, M. T., & Johannsen, K. (2012). On the time scales of nonlinear instability in miscible displacement porous media flow. *Computational Geosciences*, *16*, 901–911. <https://doi.org/10.1007/s10596-012-9294-2>
- Emami-Meybodi, H. (2017). Stability analysis of dissolution-driven convection in porous media. *Physics of Fluids*, *29*, 014102. <https://doi.org/10.1063/1.4974275>
- Emami-Meybodi, H., Hassanzadeh, H., Green, C. P., & Ennis-King, J. (2015). Convective dissolution of CO<sub>2</sub> in saline aquifers: Progress in modeling and experiments. *International Journal of Greenhouse Gas Control*, *40*, 238–266. <https://doi.org/10.1016/j.ijggc.2015.04.003>
- Ennis-King, J., & Paterson, L. (2005). Role of convective mixing in the long-term storage of carbon dioxide in deep saline formations. *SPE Journal*, *10*, 349–356. <https://doi.org/10.2118/84344-PA>
- Ennis-King, J., Preston, I., & Paterson, L. (2005). Onset of convection in anisotropic porous media subject to a rapid change in boundary conditions. *Physics of Fluids*, *17*, 084107. <https://doi.org/10.1063/1.2033911>
- Farajzadeh, R., Salimi, H., Zitha, P. L. J., & Bruining, H. (2007). Numerical simulation of density-driven natural convection in porous media with application for CO<sub>2</sub> injection projects. *International Journal of Heat and Mass Transfer*, *50*, 5054–5064. <https://doi.org/10.1016/j.ijheatmasstransfer.2007.08.019>
- Fu, Y. C., & Liu, Y. (2016). Development of a robust image processing technique for bubbly flow measurement in a narrow rectangular channel. *International Journal of Multiphase Flow*, *84*, 217–228. <https://doi.org/10.1016/j.ijmultiphaseflow.2016.04.011>
- Guo, R. C., Dalton, L. E., Fan, M., McClure, J., Zeng, L., Crandall, D., & Chen, C. (2020). The role of the spatial heterogeneity and correlation length of surface wettability on two-phase flow in a CO<sub>2</sub>-water-rock system. *Advances in Water Resources*, *146*, 103763. <https://doi.org/10.1016/j.advwatres.2020.103763>
- Hassanzadeh, H., Pooladi-Darvish, M., & Keith, D. W. (2006). Stability of a fluid in a horizontal saturated porous layer: Effect of non-linear concentration profile, initial, and boundary conditions. *Transport in Porous Media*, *65*, 193–211. <https://doi.org/10.1007/s11242-005-6088-1>
- Horton, C. W., & Rogers, F. T. (1945). Convection currents in a porous medium. *Journal of Applied Physics*, *16*, 367–370. <https://doi.org/10.1063/1.1707601>
- House, K. Z., Schrag, D. P., Harvey, C. F., & Lackner, K. S. (2006). Permanent carbon dioxide storage in deep-sea sediments. *Proceedings of the National Academy of Sciences of the United States of America*, *103*, 12291–12295. <https://doi.org/10.1073/pnas.0605318103>
- Javaheri, M., Abedi, J., & Hassanzadeh, H. (2010). Linear stability analysis of double-diffusive convection in porous media, with application to geological storage of CO<sub>2</sub>. *Transport in Porous Media*, *84*, 441–456. <https://doi.org/10.1007/s11242-009-9513-z>
- Jeffreys, H. (1926). The stability of a layer of fluid heated below. *Philosophical Magazine*, *2*, 833–844. <https://doi.org/10.1080/14786442608564114>
- Kim, M. C. (2013). Onset of buoyancy-driven convection in a fluid-saturated porous medium bounded by a long cylinder. *Transport in Porous Media*, *97*, 395–408. <https://doi.org/10.1007/s11242-013-0130-5>
- Kim, M. C. (2014a). Onset of buoyancy-driven convection in a liquid-saturated cylindrical anisotropic porous layer supported by a gas phase. *Transport in Porous Media*, *102*, 31–42. <https://doi.org/10.1007/s11242-013-0259-2>
- Kim, M. C. (2014b). Onset of buoyancy-driven convection in a variable viscosity liquid saturated in a porous medium. *Chemical Engineering Science*, *113*, 77–87. <https://doi.org/10.1016/j.ces.2014.04.012>
- Kim, M. C., & Choi, C. K. (2012). Linear stability analysis on the onset of buoyancy-driven convection in liquid-saturated porous medium. *Physics of Fluids*, *24*, 044102. <https://doi.org/10.1063/1.3703330>
- Kim, M. C., Song, K. H., Choi, C. K., & Yeo, J.-K. (2008). Onset of buoyancy-driven convection in a liquid-saturated cylindrical porous layer supported by a gas layer. *Physics of Fluids*, *20*, 054104. <https://doi.org/10.1063/1.2919737>
- Kneafsey, T. J., & Pruess, K. (2010). Laboratory flow experiments for visualizing carbon dioxide-induced, density-driven brine convection. *Transport in Porous Media*, *82*, 123–139. <https://doi.org/10.1007/s11242-009-9482-2>
- Kovscek, A. R., & Wang, Y. (2005). Geologic storage of carbon dioxide and enhanced oil recovery. I. Uncertainty quantification employing a streamline based proxy for reservoir flow simulation. *Energy Conversion and Management*, *46*, 1920–1940. <https://doi.org/10.1016/j.enconman.2004.09.008>
- Lapwood, E. R. (1948). Convection of a fluid in a porous medium. *Proceedings of the Cambridge Philosophical Society*, *44*, 508–521. <https://doi.org/10.1017/S030500410002452x>
- Liyanage, R., Cen, J., Krevor, S., Crawshaw, J. P., & Pini, R. (2019). Multidimensional observations of dissolution-driven convection in simple porous media using X-ray CT scanning. *Transport in Porous Media*, *126*, 355–378. <https://doi.org/10.1007/s11242-018-1158-3>
- Mahmoodpour, S., Rostami, B., Soltanian, M. R., & Amooie, M. A. (2019). Convective dissolution of carbon dioxide in deep saline aquifers: Insights from engineering a high-pressure porous visual cell. *Physical Review Applied*, *12*, 034016. <https://doi.org/10.1103/PhysRevApplied.12.034016>

- Meulenbroek, B., Farajzadeh, R., & Bruining, H. (2013). The effect of interface movement and viscosity variation on the stability of a diffusive interface between aqueous and gaseous CO<sub>2</sub>. *Physics of Fluids*, 25, 074103. <https://doi.org/10.1063/1.4813072>
- Moghaddam, R. N., Rostami, B., Pourafshary, P., & Fallahzadeh, Y. (2012). Quantification of density-driven natural convection for dissolution mechanism in CO<sub>2</sub> sequestration. *Transport in Porous Media*, 92, 439–456. <https://doi.org/10.1007/s11242-011-9911-x>
- Mojtaba, S., Behzad, R., Rasoul, N. M., & Mohammad, R. (2014). Experimental study of density-driven convection effects on CO<sub>2</sub> dissolution rate in formation water for geological storage. *Journal of Natural Gas Science and Engineering*, 21, 600–607. <https://doi.org/10.1016/j.jngse.2014.09.020>
- Neufeld, J. A., Hesse, M. A., Riaz, A., Hallworth, M. A., Tchelepi, H. A., & Huppert, H. E. (2010). Convective dissolution of carbon dioxide in saline aquifers. *Geophysical Research Letters*, 37. <https://doi.org/10.1029/2010GL044728>
- Newell, D. L., Carey, J. W., Backhaus, S. N., & Lichtner, P. (2018). Experimental study of gravitational mixing of supercritical CO<sub>2</sub>. *International Journal of Greenhouse Gas Control*, 71, 62–73. <https://doi.org/10.1016/j.ijggc.2018.02.013>
- Pau, G. S. H., Bell, J. B., Pruess, K., Almgren, A. S., Lijewski, M. J., & Zhang, K. (2010). High-resolution simulation and characterization of density-driven flow in CO<sub>2</sub> storage in saline aquifers. *Advances in Water Resources*, 33, 443–455. <https://doi.org/10.1016/j.advwatres.2010.01.009>
- Rayleigh, L. (1916). On convection currents in a horizontal layer of fluid, when the higher temperature is on the under side. *Philosophical Magazine*, 32, 529–546. <https://doi.org/10.1080/14786441608635602>
- Riaz, A., Hesse, M., Tchelepi, H. A., & Orr, F. M. (2006). Onset of convection in a gravitationally unstable diffusive boundary layer in porous media. *Journal of Fluid Mechanics*, 548, 87–111. <https://doi.org/10.1017/S0022112005007494>
- Sahu, C. K., & Neufeld, J. A. (2020). Dispersive entrainment into gravity currents in porous media. *Journal of Fluid Mechanics*, 886. <https://doi.org/10.1017/jfm.2019.1049>
- Sathaye, K. J., Hesse, M. A., Cassidy, M., & Stockli, D. F. (2014). Constraints on the magnitude and rate of CO<sub>2</sub> dissolution at Bravo Dome natural gas field. *Proceedings of the National Academy of Sciences of the United States of America*, 111, 15332–15337. <https://doi.org/10.1073/pnas.1406076111>
- Shi, Z., Wen, B., Hesse, M. A., Tsotsis, T. T., & Jessen, K. (2018). Measurement and modeling of CO<sub>2</sub> mass transfer in brine at reservoir conditions. *Advances in Water Resources*, 113, 100–111. <https://doi.org/10.1016/j.advwatres.2017.11.002>
- Slim, A. C. (2014). Solutal-convection regimes in a two-dimensional porous medium. *Journal of Fluid Mechanics*, 741, 461–491. <https://doi.org/10.1017/jfm.2013.673>
- Slim, A. C., Bandi, M. M., Miller, J. C., & Mahadevan, L. (2013). Dissolution-driven convection in a Hele-Shaw cell. *Physics of Fluids*, 25, 024101. <https://doi.org/10.1063/1.4790511>
- Slim, A. C., & Ramakrishnan, T. S. (2010). Onset and cessation of time-dependent, dissolution-driven convection in porous media. *Physics of Fluids*, 22, 124103. <https://doi.org/10.1063/1.3528009>
- Taheri, A., Lindeberg, E., Torsæter, O., & Wessel-Berg, D. (2017). Qualitative and quantitative experimental study of convective mixing process during storage of CO<sub>2</sub> in homogeneous saline aquifers. *International Journal of Greenhouse Gas Control*, 66, 159–176. <https://doi.org/10.1016/j.ijggc.2017.08.023>
- Wen, B. L., Akhbari, D., Zhang, L., & Hesse, M. A. (2018). Convective carbon dioxide dissolution in a closed porous medium at low pressure. *Journal of Fluid Mechanics*, 854, 56–87. <https://doi.org/10.1017/jfm.2018.622>
- Wessel-Berg, D. (2009). On a linear stability problem related to underground CO<sub>2</sub> storage. *SIAM Journal on Applied Mathematics*, 70, 1219–1238. <https://doi.org/10.1137/070702655>
- Xu, X. F., Chen, S., & Zhang, D. (2006). Convective stability analysis of the long-term storage of carbon dioxide in deep saline aquifers. *Advances in Water Resources*, 29, 397–407. <https://doi.org/10.1016/j.advwatres.2005.05.008>